Nanoscale

Free-Standing Large, Ultrathin Germanium Selenide van der Waals Ribbons by Combined Vapor-Liquid-Solid Growth and Edge Attachment

Journal:	*Nanoscale*
Manuscript ID	NR-ART-01-2022-000397.R1
Article Type:	Paper
Date Submitted by the Author:	18-Mar-2022
Complete List of Authors:	Sutter, Eli; University of Nebraska-Lincoln, Department of Mechanical and Materials Engineering French, Jacob; University of Nebraska-Lincoln, Electrical and Computer Engineering Sutter, Peter; University of Nebraska-Lincoln, Electrical and Computer Engineering

SCHOLARONE™
Manuscripts

Free-Standing Large, Ultrathin Germanium Selenide van der Waals Ribbons by Combined Vapor-Liquid-Solid Growth and Edge Attachment

Eli Sutter,[1,2,*] Jacob S. French,[3] and Peter Sutter[3]

[1]*Department of Mechanical and Materials Engineering, University of Nebraska-Lincoln, Lincoln, NE 68588 (USA)*
[2]*Nebraska Center for Materials and Nanoscience, University of Nebraska-Lincoln, Lincoln, NE 68588 (USA)*
[3]*Department of Electrical and Computer Engineering, University of Nebraska-Lincoln, Lincoln, NE 68588 (USA)*

ABSTRACT

Among group IV monochalcogenides, layered GeSe is of interest for its anisotropic properties, 1.3 eV direct band gap, ferroelectricity, high mobility, and excellent environmental stability. Electronic, optoelectronic and photovoltaic applications depend on the development of synthesis approaches that yield large quantities of crystalline flakes with controllable size and thickness. Here, we demonstrate the growth of single-crystalline GeSe nanoribbons by a vapor-liquid-solid process over Au catalyst on different substrates at low thermal budget. The nanoribbons crystallize in a layered structure, with ribbon axis along the armchair direction of the van der Waals layers. The ribbon morphology is determined by catalyst driven fast longitudinal growth accompanied by lateral expansion *via* edge-specific incorporation into the basal planes. This combined growth mechanism enables temperature controlled realization of ribbons with typical widths of up to 30 μm and lengths exceeding 100 μm, while maintaining sub-50 nm thickness. Nanoscale cathodoluminescence spectroscopy on individual GeSe nanoribbons demonstrates intense temperature-dependent band-edge emission up to room temperature, with fundamental bandgap and temperature coefficient of $E_g(0) = 1.29$ eV and $\alpha = 3.0\times10^{-4}$ eV/K, respectively, confirming high quality GeSe with low concentration of non-radiative recombination centers promising for optoelectronic applications including light emitters, photodetectors, and solar cells.

*Corresponding author: esutter@unl.edu

Keywords: 2D layered crystals, Germanium selenide, nanoribbons, cathodoluminescence, optoelectronics

INTRODUCTION

Group-IV monochalcogenides (MX, where M = Ge, Sn; X = S, Se) have attracted interest as semiconductors with anisotropic structure and properties, which distinguish them from other 2D semiconductors such as transition metal dichalcogenides and render them suitable for applications such as polarization-sensitive light emission and detection, valleytronics, twistronics, ferroelectric random access memory, *etc*. Among the group IV monochalcogenides, germanium selenide (GeSe) combines the anisotropic orthorhombic layered structure (responsible for highly anisotropic absorbance and polarization dependent photoresponse[1-4] and ferroelectric behavior),[5] with fast transformation between amorphous and crystalline states, low absorption losses and a significant difference between the refractive indices of the two phases, attractive for phase change memory devices.[6, 7] GeSe has a direct band gap of 1.3 eV,[8] which makes it suitable for optoelectronic applications as near-infrared photodetectors and in photovoltaics as an intrinsically p-type absorber layer material. Polycrystalline GeSe films have been incorporated in solar cells with power conversion efficiency up to 5.2%.[9, 10] Flakes[4] exfoliated from single crystals and evaporated GeSe films[9, 11] show mobilities of 3 – 15 $cm^2\ V^{-1}\ s^{-1}$. GeSe single crystals have significantly higher hole mobility >120 $cm^2\ V^{-1}\ s^{-1}$,[12] promising that single crystalline flakes might achieve such high mobilities as well. Bilayer and few-layer GeSe is predicted to have very high absorbance (>10^4 cm^{-1}, close to absorption edge), anisotropic spin transport[13] and emergence of 1D flat bands in twisted bilayers.[14] In addition, the GeSe surface is found to be virtually defect and impurity-free,[15] which combined with high air-, thermal-, humidity- and light-stability, adds to its advantages for many applications.[10]

Surprisingly, very limited reports exist of successful bottom-up synthesis approaches for nanostructures of orthorhombic GeSe. Solution synthesis has yielded GeSe nanosheets with few micrometer lateral size[16] that could be relatively thick (300 – 400 nm),[17] as well as thin, long GeSe nanobelts.[18] Vapor transport growth of GeSe flakes should be straightforward since GeSe evaporates as a molecule and has high vapor pressure at relatively low temperatures, similar to other group IV-monochalcogenides, which has allowed the controlled synthesis of GeS[19] and SnS flakes[20, 21] as well as heterostructures between them[22, 23] under mild conditions. However, vapor transport growth using stoichiometric GeSe as a precursor has been carried out mostly at high source temperatures (T_S) with mixed results to date, including the formation of massive nano-combs (T_S = 570°C),[24, 25] sub-μm triangular plates with tens of nm thickness (470°C),[26] standing hexagonal plates with ~15 nm thickness and lateral sizes of a few μm (550°C),[2] and ribbons of a hexagonal GeSe polymorph (550°C).[27] Recent attempts to reduce the thermal budget of the vapor source (T_S = 430°C) yielded complete films consisting of standing grains on SiO_2.[28] Alternative precursors such as GeI_2 and H_2Se give rise to thick, μm-sized flakes,[29] while $GeSe_2$ and H_2 have produced few-μm sized flakes with thicknesses as low as 5 nm (550°C).

Here we demonstrate the controlled formation of GeSe nanoribbons, mass-produced as dense forests by a vapor-liquid-solid (VLS) growth process over Au catalyst on different substrates, including Au, graphite, and NaCl, and at lower source temperatures. Transmission electron microscopy (TEM), energy dispersive X-ray spectroscopy (EDS) and mapping, micro-Raman spectroscopy and atomic force microscopy (AFM) are used to investigate the structure, chemical composition, crystallinity, morphology and

thickness of the nanoribbons. These investigations show that synthesized ribbons are single-crystalline with typical widths of several μm, uniform thickness below 50 nm, lengths often reaching or exceeding 100 μm, and smooth top and bottom facets. Nanoscale scanning TEM (STEM) cathodoluminescence spectroscopy on individual single crystalline GeSe nanoribbons shows intense temperature-dependent band edge emission promising for optoelectronic applications including light emitters, photodetectors, and solar cells.

RESULTS AND DISCUSSION

GeSe nanoribbons were grown in a two-zone tube furnace by GeSe vapor transport on Si(100) substrates covered by a thin (2-5 nm) Au film (see Methods for details). At substrate temperatures between 280 – 340°C, we obtain a high density of ribbon-like nanostructures on Au-covered Si substrates (Fig. 1 (a); Fig S1). Scanning electron microscopy (SEM) of the ensembles as well as of individual nanoribbons transferred to flat SiN_x/Si substrates (Fig. 1 (c)) show that the ribbons are bounded by sharp edges and are strongly tapered. The widths of the ribbons can reach 20 μm, and their lengths after transfer are usually several tens of μm but could be significantly longer on the growth substrate. SEM-EDS spectra (Fig. 1 (b)), measured directly on the nanoribbon forest on the growth substrate (Fig. S2) and on transferred individual ribbons (Fig.1 (c)), show that the nanostructures consist entirely of Ge and Se. Quantification of the spectra confirms a Ge:Se atomic ratio of ~1:1, corresponding to GeSe. EDS elemental maps show a uniform distribution of Ge and Se across the nanoribbons (Fig. 1 (c); Fig. S3), as well as relatively small attenuation of the Si signal from the support, suggesting a small thickness.

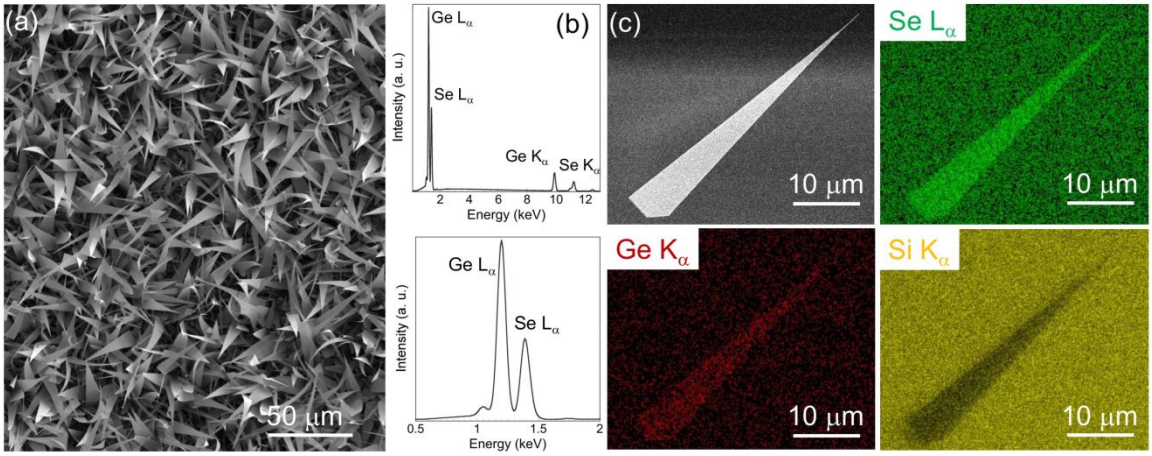

Figure 1. Morphology and composition of GeSe nanoribbons. **(a)** SEM of Au-catalyzed GeSe nanoribbons on the Au/Si growth substrate. **(b)** EDS spectrum of the ensemble of GeSe nanoribbons (top) and zoomed-in spectrum in the range between 1.5 – 2 keV (bottom), yielding a composition of 52.8 at.% Ge and 47.2 at% Se. **(c)** SEM image and EDS chemical maps of a characteristic GeSe nanoribbon transferred to SiN_x/Si support showing the distribution of Ge (red), Se (green) and Si (yellow).

TEM and high-angle annular dark field scanning TEM (HAADF-STEM) images (Fig. 2 (a), (b); Fig. S4) show large individual nanoribbons with lengths up to several tens of μm. The ribbons show a characteristic darker TEM contrast at the tip (Fig 2 (a), inset) consistent with the Au catalyst particle with higher average atomic number, Z. Electron diffraction (Fig. 2 (c); Fig. S4) confirms that these ribbons consist of monocrystalline layered GeSe (orthorhombic, space group Pnma, $\boldsymbol{a}$ = 3.878 Å, $\boldsymbol{b}$ = 4.5499 Å, $\boldsymbol{c}$ = 11.142 Å, JCPDS No. 48-1226).[30] All the ribbons are viewed along the [001] zone axis (ZA). This basal-plane imaging (ZA [001]) confirms that the $\boldsymbol{c}$-axis (*i.e.*, the van der Waals stacking direction) is perpendicular to the ribbon axis, similar to GaS and GaSe nanoribbons reported earlier.[31, 32] In addition, electron diffraction patterns show that the symmetry axis of the ribbons is oriented along the [010] crystallographic direction. High-resolution TEM imaging (Figure 2 (c), S4) shows the characteristic atomic structure of the GeSe basal plane and comparison to multislice simulations confirms the high crystal

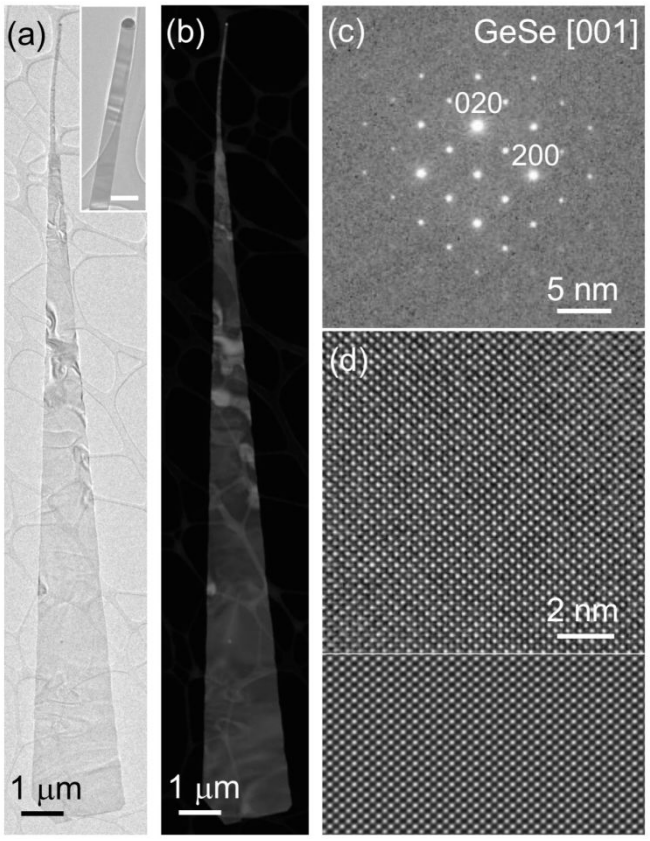

Figure 2. Morphology of single GeSe nanoribbons. (a) TEM image of a characteristic GeSe nanoribbon transferred to carbon TEM grid (growth temperature: 320°C). Inset: TEM image of the ribbon in the vicinity of the Au tip. Scale bar: 100 nm. **(b)** HAADF-STEM image of the nanoribbon shown in (a). **(c)** Electron diffraction pattern of the GeSe ribbon, viewed along the [001] zone axis. **(d)** High-resolution TEM image of the GeSe ribbon (top), and multi-slice image simulation (bottom).

quality of the GeSe ribbons. Therefore, the TEM investigation of the ribbons grown on Au/Si demonstrates that they consist of single-crystalline GeSe with layer stacking (***c***-axis) perpendicular to the ribbon axis, grown along the [010] direction (***b***-axis, *i.e.*, armchair direction). We find the same ribbon morphology and stacking orientation, independent of the substrate. TEM and electron diffraction of ribbons grown on Au-covered graphite and NaCl (Figs. S5 and S7) show identical single-crystalline structure and basal-plane orientation as ribbons grown on Au/Si substrates. Importantly, the size of the ribbons can be efficiently controlled by the synthesis temperature; increasing the substrate temperature leads to an increase of the lateral size of the ribbons to 20 μm or

more, while preserving their morphology and layer stacking (Figs. S5 and S7), and only minimally increasing their thickness.

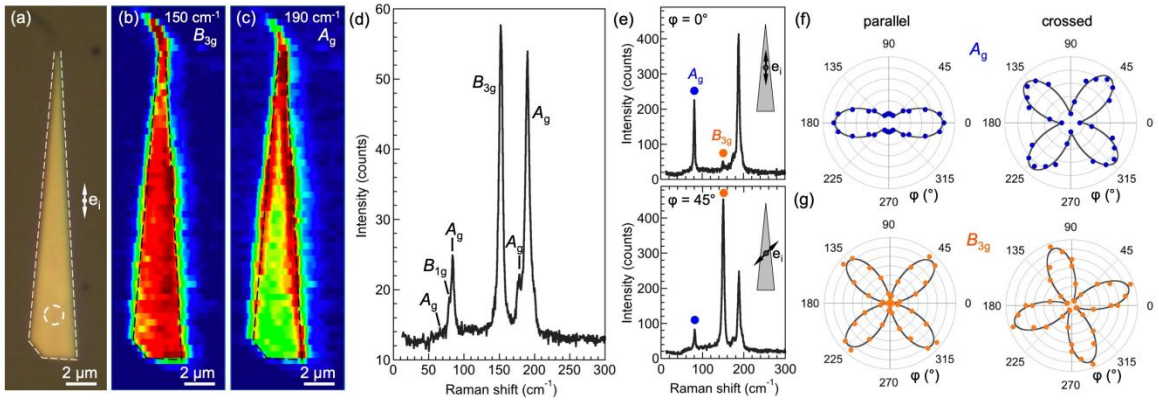

Figure 3. Raman spectroscopy of GeSe nanoribbons. (a) Optical microscopy of a GeSe nanoribbon grown at 320°C. Arrow: Polarization axis for φ = 0° in polarized Raman measurements (see (e) - (g)). **(b), (c)** Examples of micro-Raman intensity maps of A_g and B_{3g} Raman modes of GeSe. Dashed lines trace edge of the nanoribbon shown in (a). **(d)** Raman spectrum of the GeSe ribbon, obtained at the location of the circled area in (a). **(e)** Polarized Raman spectra for incident polarization along the ribbon axis (0°, top) and at 45° (bottom). **(f), (g)** Polar plots of the polarization-dependent intensity of the GeSe Raman modes at 85 cm^{-1} (A_g) and 150 cm^{-1} (B_{3g}), respectively. Spectra were obtained with linearly polarized incident light with variable polarization axis (angle φ) relative to the (***a***, ***b***) crystal axes of the GeSe ribbon (see (e)). Plots on the left and right represent data obtained with scattered-light analyzer aligned (parallel) and perpendicular (crossed) to the incident polarization. Solid lines represent fits of the measured peak intensities, $I = k^2(\sin 2\varphi)^2$ for B_{3g} (parallel) and $I = (m \cos^2\varphi + n \sin^2\varphi)^2$ for A_g and B_{3g} (crossed).

Micro-Raman spectroscopy further confirms the uniformity of the single-crystalline GeSe ribbons. Orthorhombic GeSe has eight atoms per primitive unit cell forming puckered double-layers perpendicular to the ***c***-axis. It has 21 optical phonon modes, 12 of which are Raman active with A_g, B_{1g}, and B_{3g} symmetry.[33] The Raman spectrum of a characteristic nanoribbon (Fig. 3 (d)) shows peaks corresponding to the A_g, B_{1g}, and B_{3g} Raman modes of GeSe. Raman intensity maps of the major Raman-active modes (Fig. 3 (b), (c); Fig. S8) show a homogeneous intensity distribution inside the ribbons for modes with B_{3g} symmetry, whereas all A_g modes have highest intensity near the nanoribbon edges. These differences correlate with the different displacement patterns of the two

types of phonon modes. B_{3g} modes involve atom displacements in the (***a***, ***c***) plane (*i.e.*, perpendicular to the armchair ribbon axis), while in A_g modes the atoms vibrate in the (***b***, ***c***) plane (*i.e.*, parallel to the ribbon edges). Polarized Raman spectroscopy confirms highly anisotropic vibrational modes (Fig. 3 (e)-(g)), consistent with single crystalline GeSe nanoribbons with anisotropic (orthorhombic) layered structure.[4]

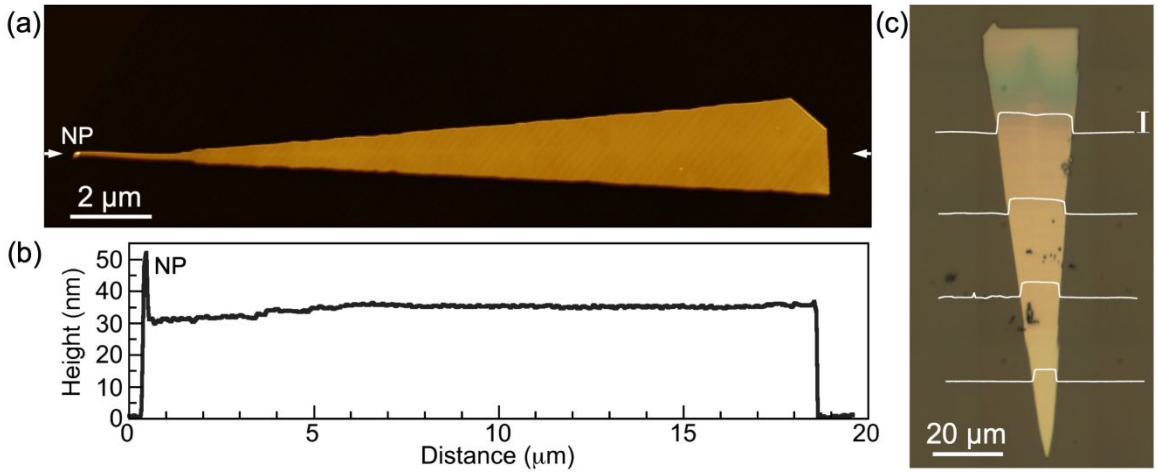

Figure 4. AFM characterization of GeSe nanoribbons grown at temperatures between 280 - 340°C over Au VLS catalyst and dry-transferred onto a SiN_x/Si chip. (a) AFM image of a typical nanoribbon grown at 320°C. **(b)** Height profile along the line between arrows in (a). NP: the Au catalyst nanoparticle at the tip of the nanoribbon. **(c)** Optical image of a nanoribbon grown at 340°C, along with a series of thickness profiles obtained at regular intervals along the ribbon. No ribbons with thickness exceeding 100 nm were found on this sample. Height scale bar (top right): 50 nm.

Atomic force microscopy (AFM) demonstrates that the Au-catalyzed GeSe ribbons grown in the temperature range between 280 – 340°C have flat top/bottom facets (Figure 3). The thickness of the ribbons remains constant over tens of microns of length. Usually, the thickness decreases slightly in the ribbon segment directly adjacent to the tip. The AFM measurements also resolve clearly the Au catalyst nanoparticles (NP) at the tips of the GeSe ribbons. In general, GeSe ribbons grown at temperatures below 320°C are less than 40 nm thick (Fig. 3 (a), (b)). At higher temperatures, the thickness of the ribbons

increases slightly but remains below 50 nm, despite a significant increase in lateral size (length > 120 μm, base width 30 μm, see Fig. 3 (c), S1 (c)).

We have demonstrated the synthesis of single-crystalline GeSe nanoribbons using vapor transport of GeSe at source temperatures of 420-450°C on Si, graphite and NaCl substrates covered with thin Au films. Growth performed under identical conditions on Si substrates without Au catalyst resulted in the formation of standing GeSe flakes with irregular shapes (Fig. S12), and with significantly smaller sizes. This finding is similar to earlier results.[28] These observations in combination with the invariable presence of Au particles at the tips of the GeSe ribbons suggest that the growth proceeds *via* a VLS mechanism. Similar to the VLS growth of other van der Waals nanostructures, such as GeS nanowires[34] and GaSe nanoribbons,[31] the GeSe precursor used here appears to combine with Au nanoparticles to form a (quasi-) binary eutectic, which acts as the active VLS catalyst in the growth of GeSe nanoribbons. Generally, we can distinguish two possible scenarios for the growth of the GeSe ribbons: (i) pure VLS growth, in which fast-growing ribbons maintain constant lateral dimensions defined by the size of the catalyst drop; or (ii) VLS catalyst driven longitudinal growth accompanied by non-specific incorporation into the exposed edges of the basal planes. The former is frequently observed in the growth of conventional and van der Waals nanowires, where the molten catalyst drop either maintains a constant diameter or progressively increases in size by intake of off-stoichiometric components in the supplied vapor, thus giving rise to straight[31, 35] or tapered[32] nanowires or –ribbons, respectively. The second scenario – concurrent VLS elongation and non-specific edge incorporation from the vapor phase – leads to a tapered shape due to the different exposure duration of the edges near the base

and tip of the nanostructures.[35] The growth of our GeSe nanoribbons appear to follows this second growth scenario. While AFM shows negligible increase in the thickness of GeSe ribbons during growth over several tens of microns of length, due to the cost of nucleating additional layers, the projected shape – characterized by a linearly increasing width from the front part toward the base – shows the expected fixed ratio between longitudinal and lateral growth rates by Au-catalyzed VLS and non-specific edge incorporation, respectively. As shown in Fig. S9, we can use the measured shape to determine this ratio. Opening angles of the triangular ribbons of (9.3 ± 1.5) deg translate to a ratio between VLS and non-specific growth rates of about 11.5:1 for our growth conditions. Note the narrow distributions in both cases, which indicate highly uniform rates of both VLS and non-specific edge growth across the ensembles of GeSe nanoribbons. Imaging by TEM (Fig. 2), optical microscopy (Fig. 3), and AFM (Fig. 4) show that this behavior is no longer upheld near the tip of the nanoribbons. Here, a thin segment continues at nearly unchanged width to the VLS catalyst particle, *i.e.,* there is no taper, which suggests an enhanced VLS growth rate and minimal edge incorporation. We conclude that this final section of the ribbons is likely grown during the initial cooldown where the drop in temperature reduces the solubility of the precursor in the catalyst and the catalyst expels dissolved GeSe at a high rate.

Light emission from individual GeSe nanoribbons at variable temperatures in the range 104 K – 295 K was analyzed *via* cathodoluminescence spectroscopy in high-angle annular dark-field (HAADF) STEM (STEM-CL). Panchromatic CL mapping shows bright electron-stimulated light emission uniformly across the entire nanoribbons, with highest intensity observed near the edges (Fig. 5; Fig. S10).

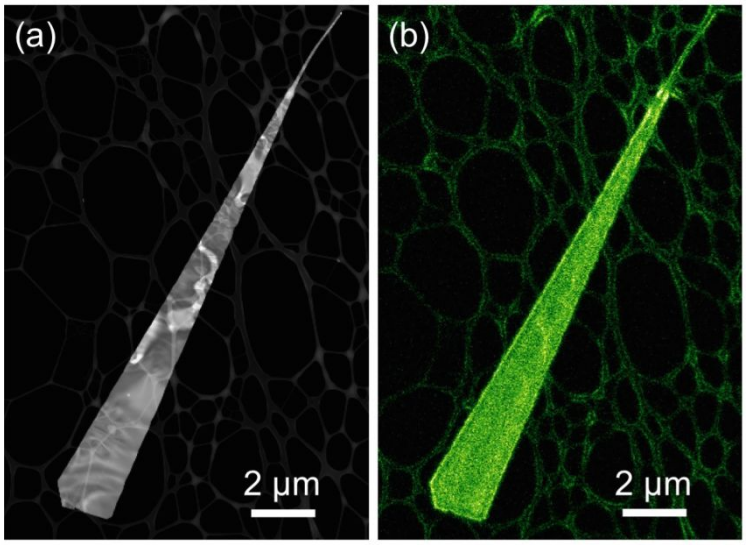

Figure 5. Nanometer-resolution electron beam excited light emission from individual GeSe nanoribbons. (a) HAADF-STEM image of a typical GeSe nanoribbon. (**b)** Corresponding panchromatic STEM-CL map (wavelength range: 400 nm ≤ λ ≤ 1000 nm).

STEM-CL measurements performed on a thicker GeSe ribbon at temperatures between 104 K – 295 K are summarized in Fig. 6. A hyperspectral linescan across a segment of the ribbon shows intense light emission with spectral component localized at the band-to-band transition energy of ~1.3 eV (Fig. 6 (c)). Individual CL spectra (Fig. 6 (d)) confirm that the CL emission consists of a single sharp peak with energy of 1.27 eV, close to the GeSe bandgap.[8] Hyperspectral linescans at the same position (arrow in Fig. 6 (b)) were measured at different temperatures. Individual CL spectra from these linescans (Fig. 6 (e)) show a systematic blue shift from the spectrum obtained at room temperature. At lower temperatures, the luminescence peaks narrow, become more intense and shifts to higher photon energy, as expected due to the increase in the bandgap at reduced temperatures.[8] The temperature-dependent luminescence of GeSe is summarized in Fig.

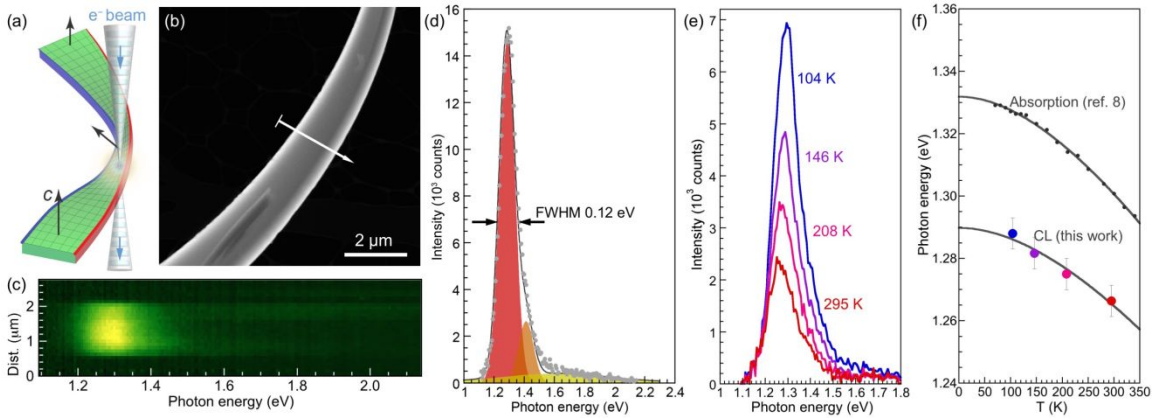

Figure 6. Cathodoluminescence spectroscopy of individual GeSe nanoribbons. (a) Schematic of a basal plane oriented, axially twisted GeSe ribbon and the exciting electron beam. **(b)** HAADF-STEM image of a section of the GeSe ribbon. **(c)** Hyperspectral CL linescan across the ribbon (arrow in (b)) measured at T = 104 K. **(d)** CL spectrum extracted from the linescan in (c). **(d)** CL spectra extracted from linescans measured at different temperatures between 104 K and room temperature. **(e)** Temperature dependence of the peak photon energy emitted by the same GeSe ribbon determined from CL measurements, compared to the temperature-dependence bandgap energy determined from optical absorption measurements.

(6 (f)). The experimental points are fitted with a Varshni relation,[36] $E_g(T) = E_g(0) + \frac{\alpha T^2}{(\beta + T)}$, where the bandgap at zero temperature, $E_g(0)$, and the constant α were left as fitting parameters and β was set to 478 K, as determined from absorption measurements.[8] The fit yields values of $E_g(0)$ = 1.29 eV and α = 3.0 × 10^{-4} eV K^{-1}. Comparison of the temperature dependence of the luminescence peak energy from our CL measurements on individual single crystalline GeSe nanoribbons to the bandgap determined by optical absorption on GeSe films[8] demonstrates identical temperature behavior, and a nearly constant offset between the luminescence and absorption data. A possible explanation for the observed ~30 meV shift of the luminescence peak to lower energy is radiative relaxation between the conduction band edge and the acceptor level due to Ge vacancies, implicated in the native p-doping of GeSe.[24] Indeed, recent electrical measurements on GeSe single crystals have suggested a relatively large acceptor activation energy of 37.8 meV,[37] in good agreement with our STEM-CL results. Overall, by showing strong

luminescence over the entire temperature range from 100 K to room temperature – in contrast to other studies that did not detect luminescence close to room temperature[26] – our spectroscopy results on single GeSe nanoribbons confirm the formation of high-quality single crystals with low concentration of defects acting as non-radiative recombination centers. These findings are promising for potential applications of our large-area nanoribbons, for example in photovoltaics.

CONCLUSIONS

We have demonstrated the facile, low-thermal budget Au-catalyzed VLS synthesis of GeSe nanoribbons with widths reaching more than 20 μm, lengths of tens of μm and thickness in the 30-50 nm range. Combined SEM, TEM, Raman, and AFM investigations demonstrate the formation of high quality single-crystalline GeSe nanoribbons with symmetry axis in the plane of the van der Waals layers. The ribbons are terminated by armchair edges, in contrast to flakes of GeS and SnS grown on substrates, which are invariantly bounded by {110} facets. We find that the ribbon morphology, stacking, and flat surfaces persist on a variety of substrates, including Si, graphite, and NaCl. Characteristic tapered shapes of the ribbons are due to the growth mechanism, which involves concurrent VLS elongation and lateral growth *via* direct edge incorporation from the vapor phase. This combined growth mechanism appears advantageous as it allows control over the sizes of the ribbons through the synthesis temperature, and realization of free-standing ribbons with predictable shapes and significant lateral sizes (length >120 μm, base width 30 μm), but thicknesses below 50 nm. STEM cathodoluminescence measurements of the optoelectronic properties of individual GeSe ribbons demonstrate intense band edge luminescence at all temperatures from 104 K up

to room temperature, confirming the high single crystal quality with low concentration of defects acting as non-radiative recombination centers.

MATERIALS AND METHODS

GeSe nanoribbons were synthesized using GeSe powder (99.99%; ALB Materials) in a pumped quartz tube reactor with two independently controlled temperature zones. The evaporation zone containing a quartz boat with the GeSe powder was heated to 420 – 450°C, while the zone containing the substrate was heated to growth temperatures of 280 – 340°C, where GeSe sublimates as a molecule. The configuration of the growth reactor is identical as in Ref. [21]. Si(100) covered with nominally 2 – 5 nm Au films deposited by sputtering at room temperature, and dewetted at the growth temperature,[38] was used as substrate. Growth was carried out under identical conditions on graphite and NaCl substrates covered with 2 – 5 nm Au films, dewetted at the growth temperature (Fig. S11). At each condition, growth was also carried out on Si control samples without deposited Au. During growth, a carrier gas (Ar, 99.9999) flow was maintained at 60 standard cubic centimeters per minute (sccm) and a pressure of 20 mTorr. Growth was typically performed for 5 minutes, resulting in the formation of GeSe nanoribbons with lengths of several tens of μms. The reactor was then cooled to room temperature naturally.

Images of the nanoribbon forests on the native growth substrates were obtained by scanning electron microscopy (SEM) in a FEI Helios Nanolab 660 field-emission microscope at 5 keV primary beam energy. SEM-EDS chemical maps were measured on nanoribbons transferred to SiN_x films on Si substrates. Structure and morphology of the nanowires were investigated by (scanning) transmission electron microscopy ((S)TEM)

and electron diffraction in an FEI Talos F200X microscope operated at 200 kV, on large ensembles of nanoribbons were dry-transferred onto lacey carbon grids. Micro-Raman spectra and maps were obtained on a Horiba Scientific XPlora Plus system with laser excitation at 532 nm at a power of 16.8 μW. Polarized Raman spectra were measured by step-wise rotation of the sample with respect to the linear polarization axis of the incident radiation without an analyzer for the scattered light. AFM imaging was performed in tapping mode on a Veeco Multimode AFM using commercial silicon nitride cantilevers with 300 kHz resonance frequency (Budget Sensors Tap300Al). STEM-CL was measured using a Gatan Vulcan holder at temperatures between 104 K and 295 K, with incident electron beam currents of ~400 pA. In panchromatic CL maps (512×512 pixels, 2 ms per pixel), broadband (400-1000 nm) light was detected by a Peltier-cooled photomultiplier detector. CL spectra were obtained using a 300 mm Czerny-Turner spectrometer and a cooled back-illuminated Si CCD detector. Hyperspectral linescans were acquired by positioning the focused electron beam in equal steps along the indicated paths and acquiring full CL spectra at each beam position (Integration time 10 s per spectrum).

ACKNOWLEDGEMENTS

This work was supported by the Department of the Navy, Office of Naval Research under ONR award number N00014-20-1-2305. The EDS measurements were performed in the Nebraska Nanoscale Facility: National Nanotechnology Coordinated Infrastructure and the Nebraska Center for Materials and Nanoscience, which are supported by the National Science Foundation under Award ECCS: 2025298, and the Nebraska Research Initiative.

Conflicts of Interest

There are no conflicts to declare.

Supporting Information

Supporting Figures S1 to S12: SEM and EDS of Au-catalyzed GeSe nanoribbons; morphology of GeSe ribbons grown with Au catalyst on different substrates; Raman spectroscopy of GeSe nanoribbons; analysis of the tapered shape of GeSe nanoribbons; cathodoluminescence spectroscopy of individual GeSe nanoribbons; TEM on dewetted gold films on graphite; TEM image of a GeSe flake grown on Si substrate without Au catalyst.

REFERENCES:

1. X. Wang, Y. Li, L. Huang, X.-W. Jiang, L. Jiang, H. Dong, Z. Wei, J. Li and W. Hu, *Journal of the American Chemical Society,* 2017, **139**, 14976-14982.
2. J. Liu, Y. Zhou, Y. Lin, M. Li, H. Cai, Y. Liang, M. Liu, Z. Huang, F. Lai, F. Huang and W. Zheng, *ACS Applied Materials & Interfaces,* 2019, **11**, 4123-4130.
3. B. Mukherjee, Y. Cai, H. R. Tan, Y. P. Feng, E. S. Tok and C. H. Sow, *ACS Applied Materials & Interfaces,* 2013, **5**, 9594-9604.
4. X. Zhou, X. Hu, B. Jin, J. Yu, K. Liu, H. Li and T. Zhai, *Advanced Science,* 2018, **5**, 1800478.
5. S. Guan, C. Liu, Y. Lu, Y. Yao and S. A. Yang, *Physical Review B,* 2018, **97**, 144104.
6. R. Soref, J. Hendrickson, H. Liang, A. Majumdar, J. Mu, X. Li and W.-P. Huang, *Optics Express,* 2015, **23**, 1536-1546.
7. J. L. Bosse, I. Grishin, Y. G. Choi, B.-k. Cheong, S. Lee, O. V. Kolosov and B. D. Huey, *Applied Physics Letters,* 2014, **104**, 053109.
8. P. A. E. Murgatroyd, M. J. Smiles, C. N. Savory, T. P. Shalvey, J. E. N. Swallow, N. Fleck, C. M. Robertson, F. Jäckel, J. Alaria, J. D. Major, D. O. Scanlon and T. D. Veal, *Chemistry of Materials,* 2020, **32**, 3245-3253.
9. W. Zi, F. Mu, X. Lu, Y. Cao, Y. Xie, L. Fang, N. Cheng, Z. Zhao and Z. Xiao, *Solar Energy,* 2020, **199**, 837-843.
10. S.-C. Liu, C.-M. Dai, Y. Min, Y. Hou, A. H. Proppe, Y. Zhou, C. Chen, S. Chen, J. Tang, D.-J. Xue, E. H. Sargent and J.-S. Hu, *Nature Communications,* 2021, **12**, 670.
11. D.-J. Xue, S.-C. Liu, C.-M. Dai, S. Chen, C. He, L. Zhao, J.-S. Hu and L.-J. Wan, *Journal of the American Chemical Society,* 2017, **139**, 958-965.
12. G. K. Solanki, M. P. Deshpande, M. K. Agarwal, P. D. Patel and S. N. Vaidya, *Journal of Materials Science Letters,* 2003, **22**, 985-987.
13. G. Shi and E. Kioupakis, *Nano Letters,* 2015, **15**, 6926-6931.
14. D. M. Kennes, L. Xian, M. Claassen and A. Rubio, *Nature Communications,* 2020, **11**, 1124.
15. Z. Jiao, Q. Yao, L. M. Balescu, Q. Liu, B. Tang and H. J. W. Zandvliet, *Surface Science,* 2019, **686**, 17-21.
16. D. D. Vaughn, R. J. Patel, M. A. Hickner and R. E. Schaak, *Journal of the American Chemical Society,* 2010, **132**, 15170-15172.
17. D.-J. Xue, J. Tan, J.-S. Hu, W. Hu, Y.-G. Guo and L.-J. Wan, *Advanced Materials,* 2012, **24**, 4528-4533.
18. D. Vaughn, D. Sun, S. M. Levin, A. J. Biacchi, T. S. Mayer and R. E. Schaak, *Chemistry of Materials,* 2012, **24**, 3643-3649.
19. E. Sutter, B. Zhang, M. Sun and P. Sutter, *ACS Nano,* 2019, **13**, 9352-9362.
20. P. Sutter, J. Wang and E. Sutter, *Advanced Materials,* 2019, **31**, 1902166.
21. E. Sutter, J. Wang and P. Sutter, *Chemistry of Materials,* 2020, **32**, 8034-8042.
22. E. Sutter, J. Wang and P. Sutter, *ACS Nano,* 2020, **14**, 12248-12255.
23. E. Sutter, R. R. Unocic, J.-C. Idrobo and P. Sutter, *Advanced Science,***n/a**, 2103830.
24. S. M. Yoon, H. J. Song and H. C. Choi, *Advanced Materials,* 2010, **22**, 2164-2167.

25. H. Kim, Y. Son, J. Lee, M. Lee, S. Park, J. Cho and H. C. Choi, *Chemistry of Materials,* 2016, **28**, 6146-6151.
26. X. Li, X. Zhang, X. Lv, J. Pang, L. Lei, Y. Liu, Y. Peng and G. Xiang, *Nanotechnology,* 2020, **31**, 285702.
27. S. Lee, J.-E. Jung, H.-g. Kim, Y. Lee, J. M. Park, J. Jang, S. Yoon, A. Ghosh, M. Kim, J. Kim, W. Na, J. Kim, H. J. Choi, H. Cheong and K. Kim, *Nano Letters,* 2021, **21**, 4305-4313.
28. Z. Wang, M. Li, X. P. A. Gao and Z. Zhang, *ACS Applied Electronic Materials,* 2019, **1**, 2236-2243.
29. K. Yumigeta, C. Brayfield, H. Cai, D. Hajra, M. Blei, S. Yang, Y. Shen and S. Tongay, *RSC Advances,* 2020, **10**, 38227-38232.
30. A. Okazaki, *Journal of the Physical Society of Japan,* 1958, **13**, 1151-1155.
31. P. Sutter, J. S. French, L. Khosravi Khorashad, C. Argyropoulos and E. Sutter, *Nano Letters,* 2021, **21**, 4335-4342.
32. E. Sutter, J. S. French, S. Sutter, J. C. Idrobo and P. Sutter, *ACS Nano,* 2020, **14**, 6117-6126.
33. T. Fukunaga, S. Sugai, T. Kinosada and K. Murase, *Solid State Communications,* 1981, **38**, 1049-1052.
34. P. Sutter, S. Wimer and E. Sutter, *Nature,* 2019, **570**, 354-357.
35. P. Sutter, J.-C. Idrobo and E. Sutter, *Advanced Functional Materials,* 2021, **31**, 2006412.
36. Y. P. Varshni, *Physica,* 1967, **34**, 149-154.
37. Y. Kim and I.-H. Choi, *Journal of the Korean Physical Society,* 2018, **72**, 238-242.
38. E. Sutter, B. Ozturk and P. Sutter, *Nanotechnology,* 2008, **19**, 435607-435613.